In: 2023 AIAA Aviation and Aeronautics Forum and Exposition (AIAA AVIATION Forum), 12-16 June 2023, San Diego, CA
DOI: 10.2514/6.2023-3392

Design of a quasi-2D rig configuration to assess nacelle aerodynamics under windmilling conditions

Luca Boscagli*, Fernando Tejero†, Avery Swarthout‡ and David MacManus§
Centre for Propulsion Engineering, Cranfield University, Cranfield, MK43 0AL, UK

Kshitij Sabnis¶ and Holger Babinsky‖
Department of Engineering, University of Cambridge, Cambridge, CB2 1PZ, UK

Chris Sheaf**
Installation Aerodynamics, Rolls-Royce plc, Derby, DE24 8BJ, UK

Aero-engine nacelles are typically designed to fulfil both design and off-design aircraft manoeuvres. Under-off design conditions one of the objective is to avoid large flow separation either on the external cowl or within the intake that can influence aircraft and engine operability. One particular scenario is represented by a low engine mass flow regime associated with one inoperative engine, also known as a windmilling condition. Under windmilling, the boundary layer on the external cowl of the nacelle can separate either due to the interaction with shock-waves or due to notable adverse pressure gradient towards the trailing edge. Both mechanisms are computationally difficult to model and there is a need for more validation of computational fluid dynamics (CFD) methods. The aim of this work is to develop a rig configuration which will provide CFD validation data for the aerodynamics of a nacelle under representative windmilling conditions. Two flight regimes are considered, namely windmilling diversion and end-of-runway. CFD simulations of a 3D nacelle are used to determine primary aerodynamic mechanisms associated with boundary layer separation. Two rig configurations are developed and both 2D and 3D CFD analyses are used to achieve the design objectives. Overall, this work presents the design philosophy and methods that were pursued to develop a quasi-2D rig configuration representative of the aerodynamics of 3D-annular aero-engine nacelles under windmilling conditions.

Nomenclature

P_0, P	=	Total and static pressure $[Pa]$
T_0, T	=	Total and static temperature $[K]$
V_x	=	Axial velocity $[m/s]$
τ_x	=	Axial wall shear stress $[Pa]$
ρ	=	Density $[kg/m^3]$
δ_{wall}	=	Wall distance $[m]$
L_{nac}	=	Nacelle length $[m]$
F_s	=	Stratford coefficient $[-]$
s_{eq}	=	Non-dimensional equivalent curvilinear coordinate $[-]$
$I_{\overline{U}}$	=	Turbulence intensity magnitude $[\%]$
x^*	=	Non-dimensional axial coordinate of the nacelle aeroline $[-]$
$MFCR_{Div}, MFCR_{EoR}$	=	Reference mass flow capture ratios

*Research Fellow, Centre for Propulsion Engineering, Cranfield University.
†Lecturer in Propulsion Systems Design, Centre for Propulsion Engineering, Cranfield University.
‡PhD Student, Centre for Propulsion Engineering, Cranfield University.
§Professor of Propulsion Aerodynamics, Centre for Propulsion Engineering, Cranfield University.
¶Research Associate, Department of Engineering, University of Cambridge.
‖Professor of Aerodynamics, Department of Engineering, University of Cambridge, AIAA Fellow.
**Installation Aerodynamics Specialist, Installation Aerodynamics, Rolls-Royce plc.

Published by AIAA. This is the Author Accepted Manuscript issued with: Creative Commons Attribution Non-Commercial License (CC:BY:NC 4.0).
The final published version (version of record) is available online at DOI:10.2514/6.2023-3392. Please refer to any applicable publisher terms of use.

γ	=	Ratio of specific heats [−]
Subscripts		
∞	=	freestream
hi	=	nacelle highlight
in	=	inlet of CFD domain

I. Introduction

The next generation of ultra-high bypass ratio aero-engines for civil aviation applications are likely to use more compact nacelles to achieve potential fuel burn benefits [1]. Within the cruise segment, the compactness of the nacelle can reduce the overall drag of the airframe due to the reduced wetted area. However, aero-engines also need to accommodate off-design conditions under which the status (e.g., laminar or turbulent, attached or separated) of the boundary layer on the nacelle is affected by more aggressive gradient and curvature distributions for compact nacelles compared to more conventional configurations. The suitability of computational methods typically used for the aerodynamic design of aero-engine nacelles [2–4] is challenged by the complex nature of the flow field under off-design conditions. For the external cowl of the nacelle two scenarios that are typically included within the nacelle design process [5–7] are windmilling diversion and end of runway. Under these conditions one of the engines is inoperative and consequently with a low mass flow and the stagnation streamlines move further into the intake (Fig. 1). Mass Flow Capture Ratio ($MFCR = A_\infty/A_{hi}$) is a non-dimensional parameter that is used to describe the area of the ingested streamtube far upstream from the engine (A_∞, Fig. 1) relative to the nacelle highlight area (A_{hi}, Fig. 1). For a fixed nacelle geometry, the flight Mach number (M_∞), MFCR and the nacelle incidence angle (α_{nac}) determine the flow regime over the nacelle.

The windmilling diversion condition arises following particular scenarios where the aircraft is at cruise and one engine becomes inoperative. The aircraft typically reduces flight altitude (h) and flight Mach number (Table 1) to meet Extended Twin-engine Operations Performance Standards (ETOPS, [8]). The MFCR also reduces and the flow undergoes a local supersonic expansion around the nacelle intake and forebody which terminates with a near-normal shock wave. The interaction between the shock wave and the boundary layer can lead to boundary layer separation on the external cowl of the nacelle. Previous work has investigated Shock-wave Boundary Layer Interaction (SBLI) within a rig representative of an intake under high incidence [9] conditions as a function of changes in MFCR and incidence angle [10, 11], Reynolds' number [12] and surface roughness [13]. Under windmilling diversion, the characteristics of the boundary layer, the position and strength of the shock and the post-shock diffusion are significantly different and therefore the definition of a new rig configuration is needed.

The windmilling End of Runway (EoR) condition is a scenario where the engine becomes inoperative during the aircraft climb-out manoeuvre. This condition is characterized by a lower flight Mach number and higher nacelle incidence angle compared to diversion (Table 1, [14]). The flow on the nacelle cowl is subsonic and the boundary layer typically separates around the top dead centre region ($\phi = 0°$, Fig. 1) due to notable diffusion on the nacelle afterbody [6]. Hoelmer et al. [14] showed that the nacelle incidence angle at the onset of separation of the boundary layer, also referred to as critical nacelle incidence angle ($\alpha_{nac,c}$), is notably affected by changes in Reynolds number. Based on a Reynolds number ($Re_{D_{hi}}$) defined with the freestream velocity (U_∞) and the nacelle highlight diameter (D_{hi}), there can be up to about 5° change in $\alpha_{nac,c}$ for $Re_{D_{hi}} \in [2, 10] \times 10^6$ [15]. Thus, the accurate prediction of the characteristics of the boundary layer is important to determine the onset of separation on the external cowl of the nacelle. However, there is a lack in the open-source literature of a canonical test case with high quality experimental measurements to validate the CFD methods typically used within the nacelle design and optimisation [3, 6]. Overall, the aim of this work is the design of two canonical rig configurations to assess the separation onset and characteristics of the boundary layer on the external cowl of a nacelle under windmilling operating conditions.

Table 1 Summary of windmilling operating conditions

	MFCR [-]	M_∞ **[-]**	α_{nac}
Diversion	$MFCR_{Div}$	0.65	4.5°
End of runway	$MFCR_{EoR}$	0.25	20°

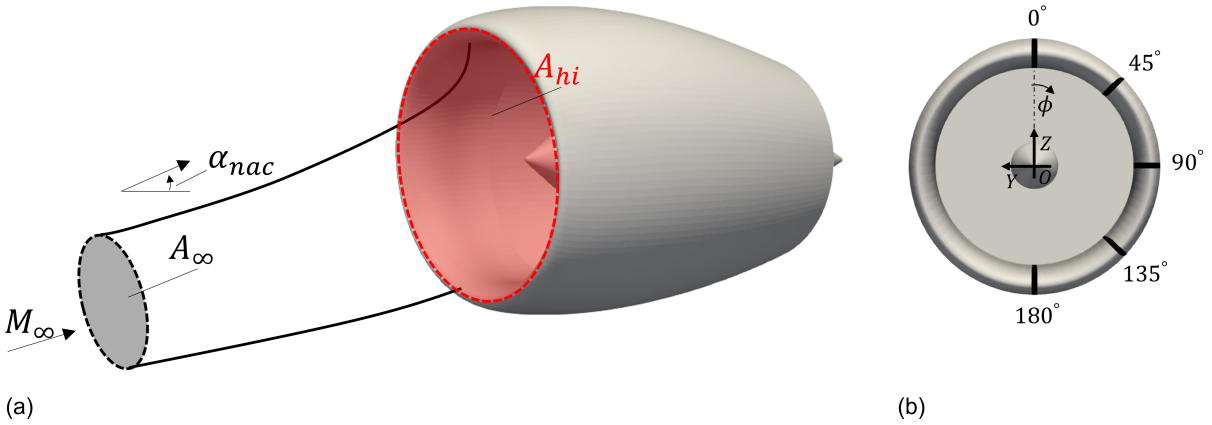


Fig. 1 (a) Schematic of the engine captured streamtube under windmilling conditions; (b) schematic of the definition of the azimuthal coordinate

II. Methodology

A double-precision density based solver with an implicit time integration formulation [16] was used for the CFD computations. The numerical fluxes were computed through a Roe scheme based on a Green-Gauss method for the spatial discretization. Reynolds Averaged Navier Stokes (RANS) equations were solved and $k\omega - SST$ [17] was used as the turbulence model. Transitional boundary layer computations ($\gamma - Re_\theta$, [16]) were also used to assess the separation characteristics of the boundary layer. A polytropic ideal gas model was used for the air and the viscosity was computed based on Sutherland's law. Three different computational models were used to firstly assess the aerodynamic of the 3D annular nacelle design and ultimately develop the quasi-2D rig configuration. A more detailed description of the design methods, CFD domain and boundary conditions used is provided in the subsequent sections.

A. 3D-annular nacelle configuration

1. Design methods

The 3D non-axisymmetric nacelle was defined with a fully parametric definition that uses the intuitive Class Shape Transformation (iCST, [18]) method. The design process was based on a multi-point, multi-objective optimisation routine [6] based on a well-established CFD methodology [3]. Different operating conditions of the flight envelope were considered for aerodynamic robustness of the down-selected configuration. These included cruise and windmilling type scenarios.

2. CFD model

The CFD model for the 3D-annular computations comprises a hemi-sphere which incorporates half-of the nacelle geometry and a symmetry plane. The spinner, intake and nacelle fan cowl are modelled as no-slip adiabatic walls and a static pressure outlet boundary condition is used at the fan face with a target mass flow that is set based on the required MFCR. The edges of the computational domain are positioned about $60D_{hi}$ upstream of the nacelle highlight and farfield boundary conditions are used to prescribe M_∞, static temperature and pressure and α_{nac}. At the farfield a turbulence intensity of 0.1% and a viscosity ratio of 1 were used. The model is grid and domain independent [3].

B. Rig configuration

1. Design intent

The rig control volume, end-points and the position of the optical access ports notably constrained the position of the nacelle aeroline within the rig and the viable design space for the upper and lower wind tunnel walls. Overall, the aerodynamic design of the rig configuration was determined as part of a set of trade-off studies to achieve 4 main objectives (Fig. 2).

1. Ensure that both attached and separated boundary layer over the forebody of the nacelle aeroline could be achieved by changing the mass flow split between upper and lower channel within the rig.
2. Match the signature of the shock over the nacelle forebody as the boundary layer moves from attached to separated for the 3D-annular configuration
3. Position the stagnation point to be approximately at the same location as the 3D-annular studies so that the growth length of the boundary layer is maintained.
4. Design the streamwise curvature distribution over the lower wall to prevent supersonic acceleration and boundary layer separation.

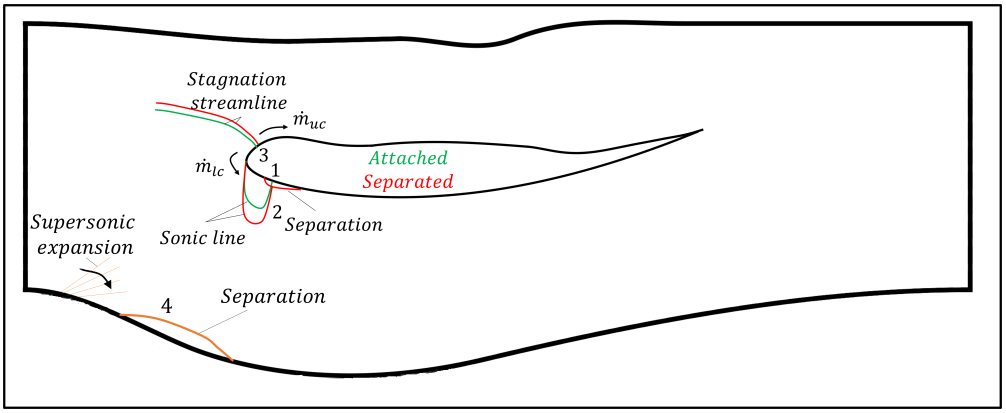


Fig. 2 Schematic of the rig design objective for development of the rig configuration

2. Design methods

A single aeroline of the 3D-annular nacelle design (Fig. 1b) was used to develop the rig configuration (Fig. 3). The design of the bounding walls is a key challenge and the switch from a 3D annular configuration to a 3D prismatic one needs to take into account the difference in the area distributions across the bounding streamtube. The rig constraints and the nomenclature are introduced in Fig. 3. The upper wall of the rig is representative of a notional streamline that is ingested within the engine captured streamtube, whereas the lower bounding wall belongs to the outer region and pass over the nacelle. The geometric definition of the lower and upper walls was fully parametric and with construction based on iCST curves [18]. The position of the nacelle aeroline within the rig was controlled through an axial (x_{off}) and a radial (r_{off}) offset as well as through a geometric incidence angle (α_g) whose centre of rotation corresponded to the centroid of a notional 3D axi-symmetric nacelle.

3. CFD models

A 2D-planar and 3D models (Fig. 4) of the rig configurations were used to determine the impact of the rig side-walls on the separation onset and characteristics of the nacelle boundary layer. The upper and lower walls of the rig were axially extruded for about twice the height of the rig inlet ($\Delta y_{in,rig}$) for numerical stability reasons. The bounding walls were modelled as adiabatic viscous walls apart from an inviscid section at the inlet of the CFD domain that was used to ensure to reproduce the likely thickness of the boundary layer at the entry of the working section ($\delta|_{x=0}$, Table 2). Total pressure ($P_{0,in}$), temperature ($T_{0,in}$) and turbulence intensity ($I_{\overline{U}}$) were prescribed at the inlet of the CFD domain (Table 2). A static pressure outlet boundary condition with an imposed target mass flow was used at the outlet of the CFD domain to achieve the desired inlet Mach number (M_{in}, Table 2). The mass flow split between upper and lower channel was controlled through a change in the area of the upper channel. Changes in the mass flow split at a fixed M_{in} were used to mimic a change in $MFCR$ by changing the position of the stagnation point on the nacelle aeroline. The changes in mass flow through the lower channel ($\dot{m}_{lc}$) were quantified relative to a reference condition ($\dot{m}_{lc,ref}$) with no separation of the boundary layer on the nacelle cowl and expressed as a percentage ($\Delta\dot{m}_{lc}$, Eq. 1). Within the design process, a porous region was positioned in the upper channel at about $0.7L_{nac}$ and it was used to mimic an increase in the area blockage to avoid generating a new grid and to speed up the whole process. Grid independence studies [19] were done for the 2D-planar model. Three grid refinements were investigated which encompassed 43×10^3, 65×10^3 and 105×10^3 nodes and $y^+ \approx 1$. The three grids were referred to as level 1, 2 and 3, respectively. A Grid Convergence

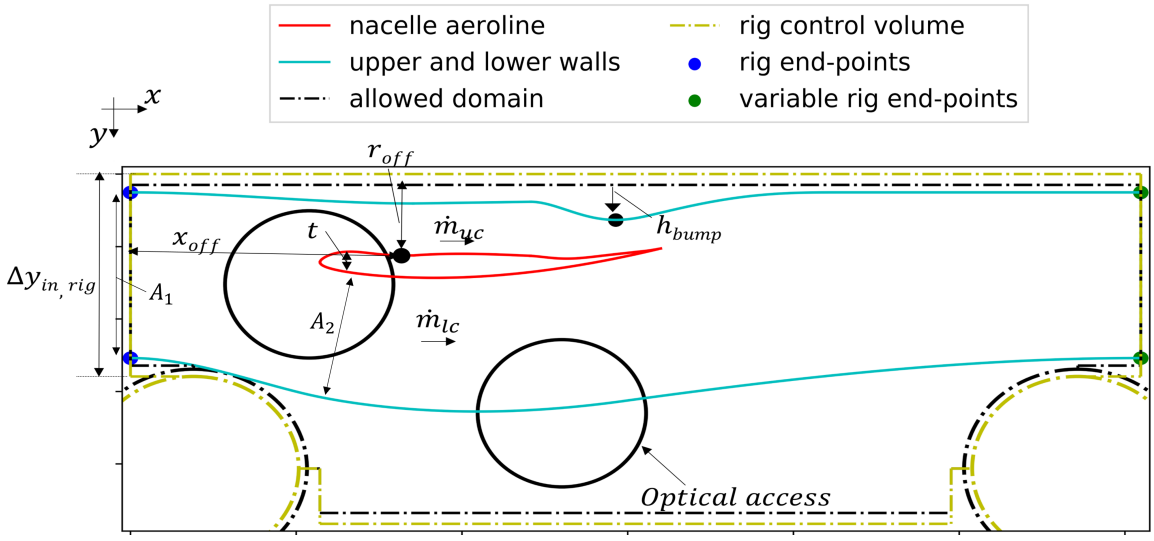


Fig. 3 Schematic of the rig configuration

Index (GCI) was computed based on the peak isentropic Mach number (M_{ise}, Eq. 2). Grid 2 had a GCI relative to level 3 grid of 0.04% and it was considered sufficiently grid independent. For the 3D model, the grid resolution in the streamwise and wall-normal directions was the same used for the 2D-planar model and there were 80 nodes in the spanwise direction. The boundary layer on the side-walls was resolved with $y^+ \approx 1$.

$$\Delta\dot{m}_{lc} = \frac{\dot{m}_{lc} - \dot{m}_{lc,ref}}{\dot{m}_{lc,ref}} \tag{1}$$

$$M_{ise} = \sqrt{\frac{2}{\gamma - 1}\left[\left(\frac{P_{0,in}}{p}\right)^{\frac{\gamma-1}{\gamma}} - 1\right]} \tag{2}$$

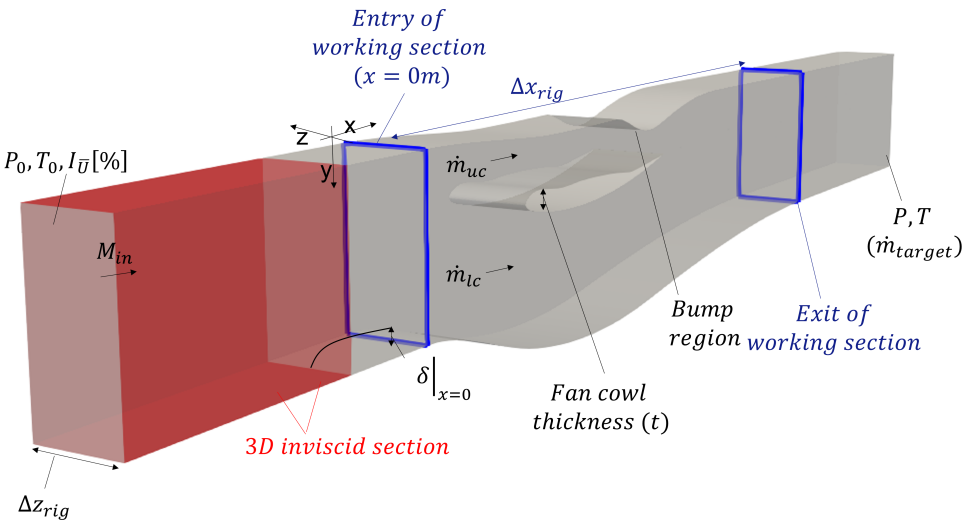


Fig. 4 Example of computational domain for 3D with side-walls computations

Table 2 Design operating point of rig configuration

	M_{in} [-]	Re_t [$\times 10^6$]	$\delta\|_{x=0}$ [mm]	$I_{\overline{U}}$ [%]
Diversion	0.65	1.15	2-3	1.0
End of runway	0.25	1.6	3-4	3.0

III. Results

A. Aerodynamics of the 3D-annular nacelle under windmilling conditions

1. Windmilling diversion

An optimized 3D annular nacelle [6] was used to define the 2D aeroline that will be used within the rig to assess the separation characteristics of the boundary layer on the nacelle fan cowl under windmilling conditions. For the candidate 3D-annular design, the effect of MFCR on the separation onset of the boundary layer was evaluated. MFCR was decreased from $MFCR_{Div} + 0.15$ to $MFCR_{Div} - 0.1$. At $MFCR_{Div}$ there was no separation on the nacelle and the peak isentropic Mach number ($M_{ise,max}$) at $\phi = 90°$ was approximately 1.6 with a near-normal shock wave located at about $0.05L_{nac}$ (Fig. 5). At $MFCR_{Div} - 0.05$ there was separation on the upper quadrant of the nacelle and the $M_{ise,max}$ increased to 1.7 at $\phi = 90°$ with the shock location unchanged.

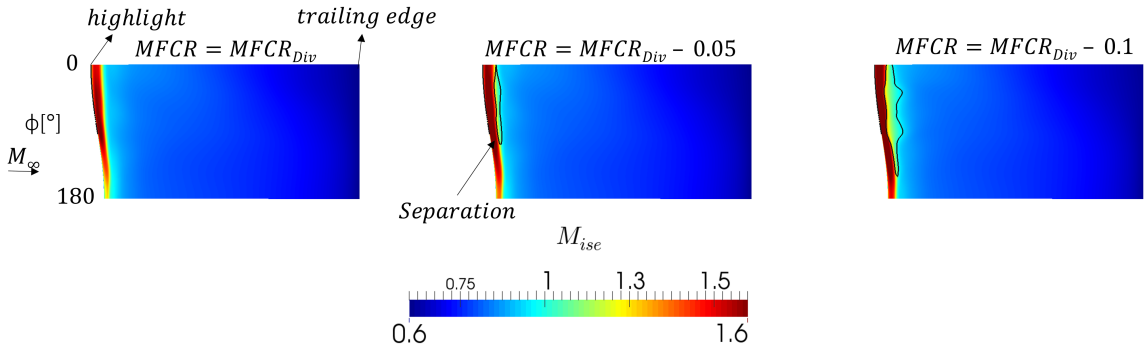


Fig. 5 Effect of $MFCR$ on the isentropic Mach number distribution on the nacelle surface at windmilling diversion. Black solid line: $\tau_x = 0$. 3D-annular model (RANS with $k\omega - SST$)

The effect of Reynolds number on the characteristics of the separation were investigated through transitional boundary layer ($\gamma - Re_\theta$) computations. A Reynolds number definition ($Re_t = \frac{U_\infty t}{\nu}$) based on the maximum thickness of the fan cowl (t, Fig. 3) and the freestream velocity (U_∞) was used. At rig size the estimated Re_t was 1.1×10^6 whereas it was about three times greater at full-size engine ($Re_t = 3.5 \times 10^6$). For both Re_t the effect of $MFCR$ on the separation onset of the boundary layer was determined (Fig. 6). At $MFCR_{Div}$ there was no separation and with a 0.05 reduction in $MFCR$ there was onset of separation on the nacelle upper quadrant ($0° < \phi < 90°$). The characteristics of the boundary layer were determined based on the intermittency function (γ, [20]). At $\phi = 90°$ there was turbulent separation for both the operating conditions ($Re_t = 3.5 \times 10^6$ and 1.1×10^6, Fig. 7). However, at the lower Re_t the transition of the boundary layer from laminar to turbulent occurred close to the onset of boundary layer separation (Fig. 7). Overall, within the range of interest for the 3D-annular computations the boundary layer was fully turbulent at the onset of separation.

2. Windmilling EoR

Under windmilling EoR condition, the effect of nacelle incidence angle on the separation onset and characteristics of the boundary layer was determined for the 3D-annular configuration. The nacelle incidence angle was progressively increased with the flight altitude and Mach number held constant. At $\alpha_{nac} = 27°$, there was no separation on the nacelle cowl and the flow was subsonic with $M_{ise,max} \approx 0.95$ (Fig. 8). With a further $1 - 2°$ increase in α_{nac}, the boundary layer on the topline region ($\phi \approx 0°$) separated on the nacelle afterbody and the separation eventually reached

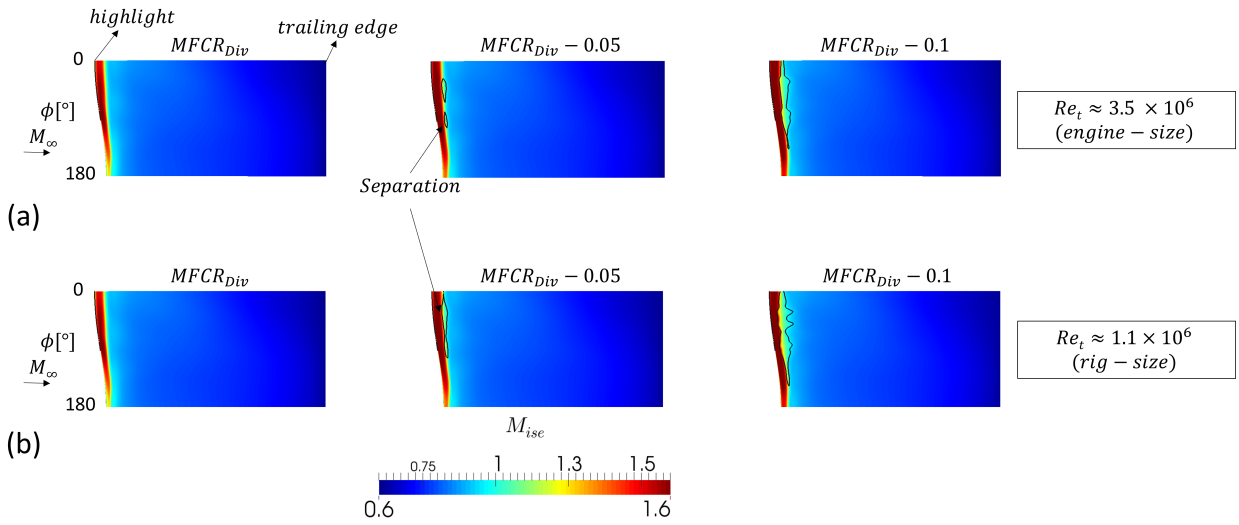


Fig. 6 Effect of $MFCR$ on the isentropic Mach number distribution on the nacelle surface at windmilling diversion. Black solid line: $\tau_x = 0$. 3D-annular model (RANS with $\gamma - Re_\theta$ turbulence model)

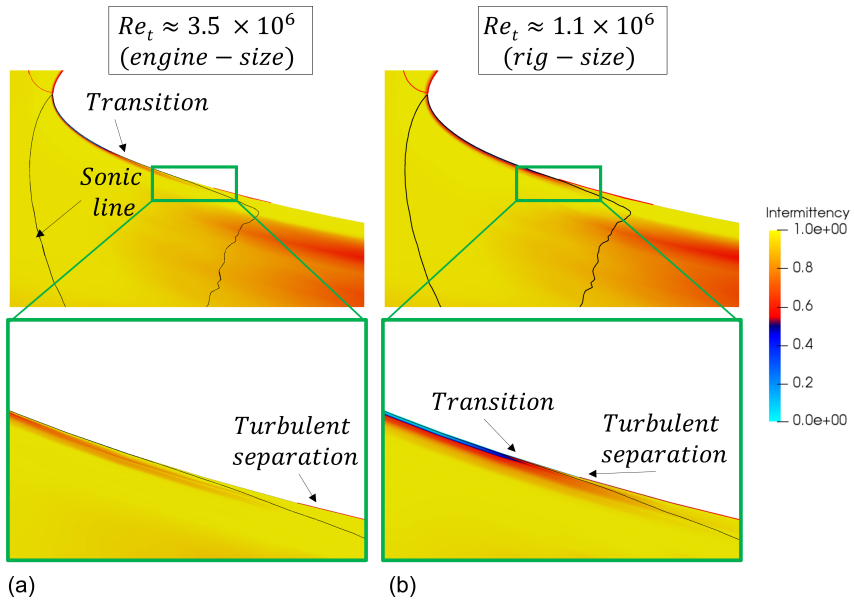


Fig. 7 Intermittency distribution on a meridional plane at $\phi = 90°$ for a nacelle under windmilling diversion conditions. $MFCR = MFCR_{Div} - 0.05$, $M_\infty = 0.65$; (a) $Re_t = 3.5 \times 10^6$ and (b) $Re_t = 1.1 \times 10^6$. Black solid line: $M = 1$. Red solid line: $V_x = 0$. 3D-annular model (RANS with $\gamma - Re_\theta$ turbulence model)

the highlight with $M_{ise,max}$ that reduced below 0.5. Under windmilling EoR, the separation of the boundary layer is diffusion driven [6] and therefore it is important to quantify the adverse pressure gradient on the nacelle cowl that needs to be achieved in the rig configuration. The Stratford coefficient (F_s, [21]) is typically used along with experimental correlation to infer the likelihood of the boundary layer to separate under an adverse pressure gradient [22]. In these circumstances, F_s was used as a surrogate of the distribution of the pressure gradient on the nacelle topline ($\phi = 0°$). An equivalent curvilinear coordinate (s_{eq}) starting from the peak suction point on the nacelle forebody was computed based on the method proposed by Cebeci et al. [23] to take into account the presence of a favourable pressure gradient on the nacelle forebody ahead of the subsonic diffusion. For the attached boundary layer ($\alpha_{nac} = 27°$), the Stratford coefficient was greater on the nacelle forebody ($s_{eq} \approx 0.1$, Fig. 9c) and it decreased approaching the nacelle trailing

edge. The latter indicated a greater amplitude of the adverse pressure gradient on the nacelle forebody compared to the nacelle afterbody. Driven by the low engine mass flow regime typical of the windmilling scenarios [6], the separation of the boundary layer rapidly progressed up to the nacelle highlight with an increase in α_{nac} and it axially extended to the full nacelle length at $\phi = 180°$. Compared to the isentropic Mach number, the axial distribution of the Stratford coefficient on the nacelle forebody was significantly more sensitive to changes in operating conditions and therefore F_s is used in the section III.B.2 as an additional metric to evaluate the link between the 3D-annular configuration and the 2D prismatic one.

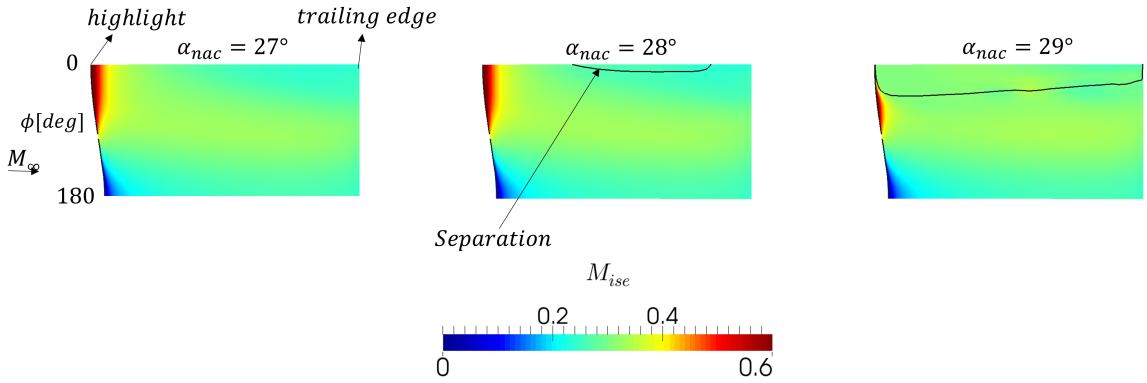


Fig. 8 Effect of α_{nac} on the isentropic Mach number distribution on the nacelle surface at windmilling EoR. Black solid line: $\tau_x = 0$. 3D-annular model (RANS with $k\omega - SST$)

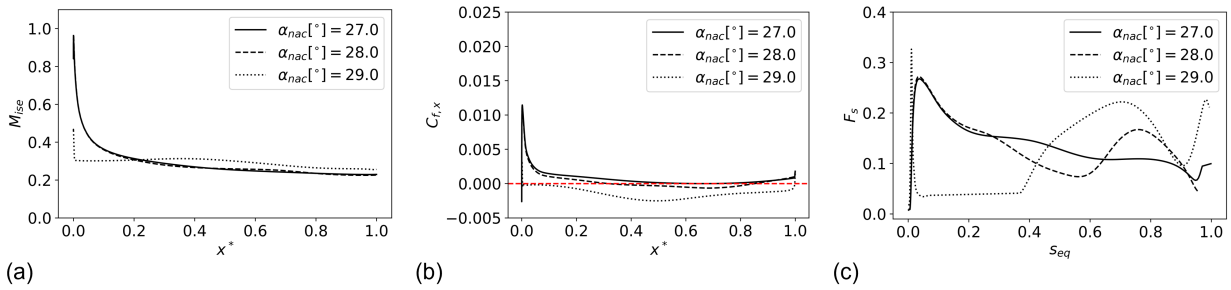


Fig. 9 Effect of α_{nac} on (a) isentropic Mach number, (b) wall axial skin friction coefficient and (c) Stratford coefficient axial distributions at $\phi = 0°$ for windmilling EoR. 3D-annular model (RANS with $k\omega - SST$)

Under the rig configuration, for fixed upper and lower rig walls, a change in the nacelle incidence angle is accompanied with a change in the mass flow split between upper and lower channel of the rig. For the 3D-annular configuration under windmilling EoR, the total pressure losses through the fan and exhaust duct as well the effect of the aircraft wing on the static pressure field at the nacelle trailing edge can significantly affect the mass flow through the engine [24] and therefore the MFCR. A further reduction in MFCR is likely to also reduce the nacelle incidence angle at which separation of the boundary layer on the nacelle occurs. The latter is typically referred to as critical nacelle incidence angle ($\alpha_{nac,c}$) and it was determined for a range of MFCR typical of the windmilling scenarios [6]. The $\alpha_{nac,c}$ varied by about 2° for the 3D candidate nacelle design and below the nominal design point ($MFCR_{EoR}$) it decreased with a reduction in $MFCR$ (Fig. 10). The latter indicated a useful range that may be investigated within the rig and which is further analysed with CFD in section III.B.2.

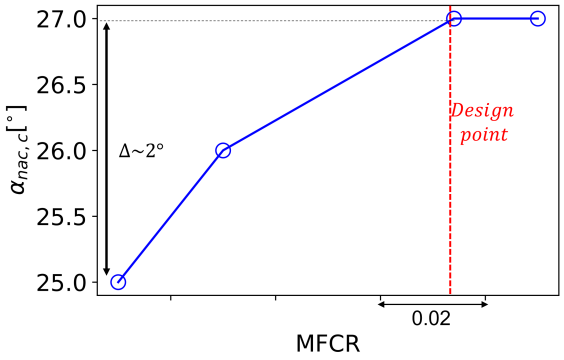


Fig. 10 Effect of MFCR on critical nacelle incidence angle $\alpha_{nac,c}$ for windmilling EoR. 3D-annular model (RANS with $k\omega - SST$)

B. Development of the rig configurations

1. Windmilling diversion

The nacelle aeroline at $\phi = 90°$ was used to model the quasi-2D flow path to be used for the experiments within the blow-down wind tunnel for the windmilling diversion scenario. The choice of the aeroline was motivated by the onset of boundary layer separation at $\phi = 90°$ for the 3D-annular configuration (Fig. 11). The aeroline was geometrically scaled down by a factor of $1/14^{th}$ relative to full-size engine to fit within the rig. The choice of the scaling factor, radial and axial position of the nacelle aeroline within the rig were part of several trade-off studies to also ensure optical access over the nacelle forebody. Overall, the design process of the rig included more than 100 configurations created and 200-300 CFD analyses. Notional inlet boundary conditions were determined both based on the full-size engine configuration as well as rig run-time and operating limits. For the diversion configuration, the minimum distance of the lower wall of the rig from the nacelle aeroline (A_2, Fig. 3) was estimated with quasi-1D isentropic flow relationships to avoid choking ($A_2 > 0.7A_1$). As the estimate did not take into account the additional area blockage due to the boundary layer growth on the wall of the rig, a few design iterations were needed. For example, for $A_2 = 0.74A_1$ there was a significant change in the signature of the shock wave when the lower channel mass flow was increased by approximately 5.9% (Fig. 12). The pre-shock Mach number slightly reduced and the shock moved forward. The latter was not representative of the 3D-annular configuration (Fig. 12) and therefore A_2 was constrained to be greater than $0.74A_1$.

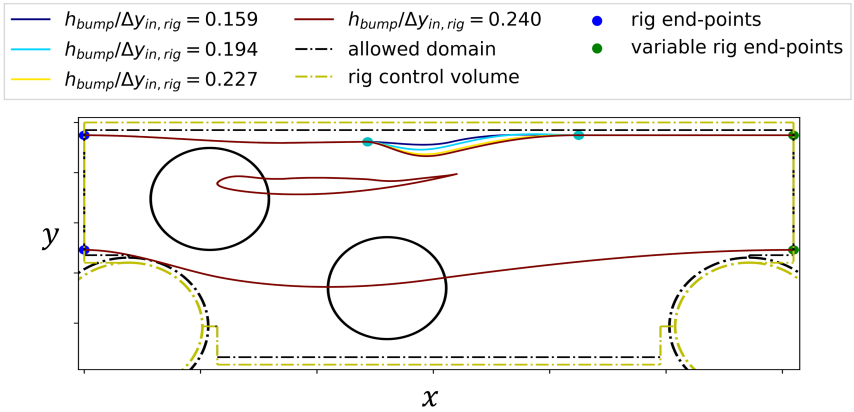


Fig. 11 Schematic of the rig configuration at diversion windmilling and bump geometries used to control the mass flow split between upper and lower channel

For the final configuration, the control of the mass flow split within the rig was achieved through a series of interchangeable bump geometries (Fig. 11). The height of the bump (h_{bump}) was defined as the minimum vertical

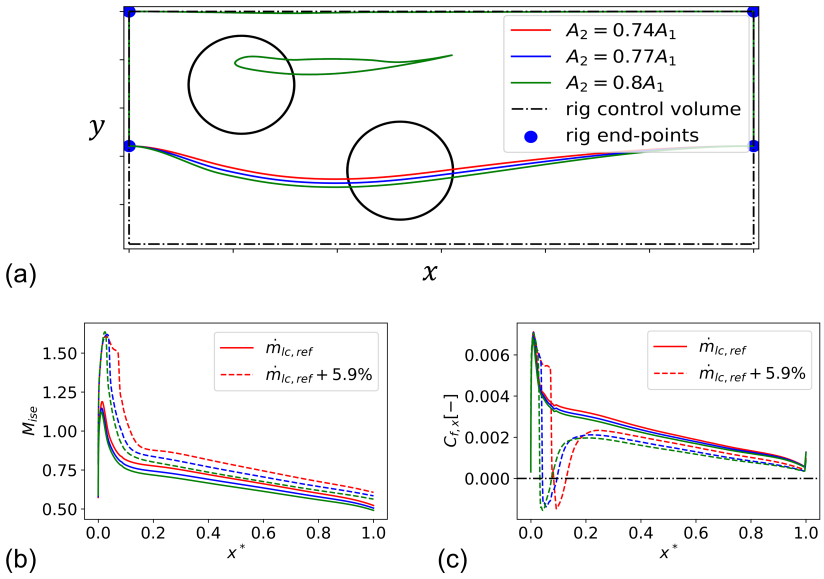


Fig. 12 Effect of changes in lower channel area (A_2) on the shock signature. (a) Geometry definition; (b) isentropic Mach number and (c) axial skin friction coefficient distributions on the nacelle forebody. $M_{in} = 0.65$; 2D-planar model with porous region in the upper channel (RANS with $k\omega - SST$ turbulence model)

distance of the nacelle aeroline from the upper wall of the rig (Fig. 11). A non-dimensional bump height ($h_{bump}/\Delta y_{in,rig}$) was defined and the different bump geometries and rig configurations were named accordingly. Four different bump geometries were used and both attached and separated conditions were assessed (Fig. 13). At the onset of separation ($h_{bump}/\Delta y_{in,rig} = 0.194$, Fig. 14), the peak isentropic Mach number on the nacelle cowl at mid-span was about 1.45. For the configurations with $h_{bump}/\Delta y_{in,rig} = 0.159$ and 0.194, the flow over the nacelle fan cowl was symmetric relative to the mid-span position ($\Delta z = 0$, Fig. 14) and it was only slightly influenced by the presence of the side-walls. For the condition $h_{bump}/\Delta y_{in,rig} = 0.227$ the flow over the fan cowl was symmetric relative to mid-span and the corner flows from the side-walls were typically confined within $5 - 10\%$ of the rig spanwise length (Fig. 13). For all the configurations there was no supersonic acceleration on the lower wall of the wind tunnel, with a peak isentropic Mach number below ≈ 0.85 and there was no boundary layer separation. Thus, the final rig configuration met the previously outlined design objectives (Fig. 2).

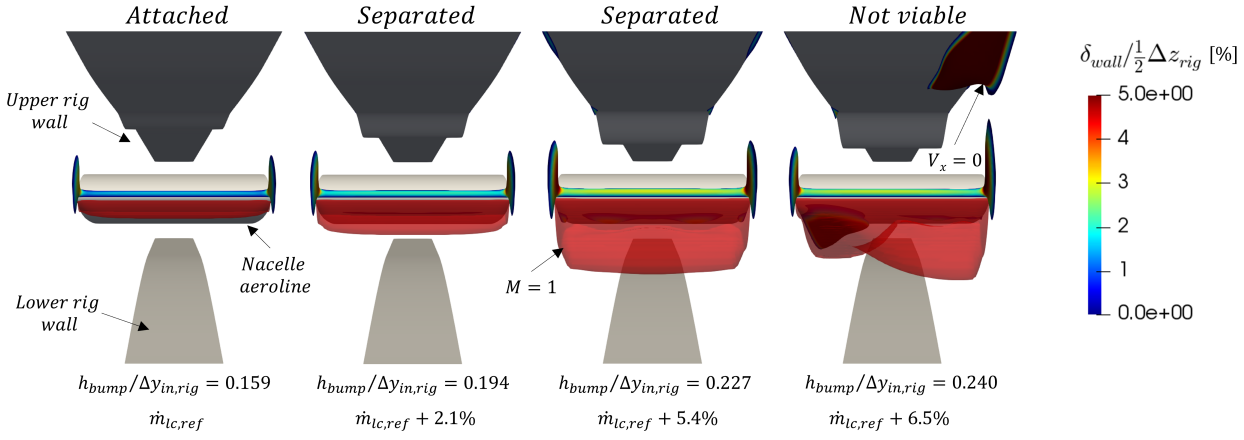


Fig. 13 Effect of a change in bump geometry on mass flow split, extent of supersonic region and separation extent. Red isosurface: $M = 1$; coloured isosurface: $V_x = 0$. $M_{in} = 0.65$; perspective view from the entry of the working section of the 3D rig configuration with side-walls (RANS with $k\omega - SST$ turbulence model)

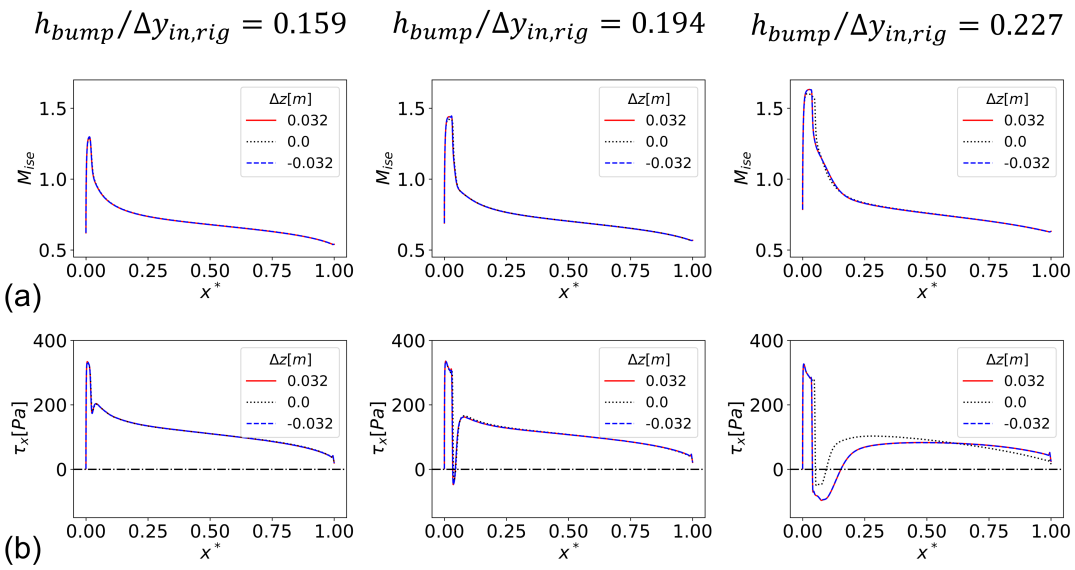


Fig. 14 Effect of a change in bump geometry on (a) isentropic Mach number and (b) axial wall shear stress distributions on the nacelle fan cowl at different spanwise positions relative to mid-span ($\Delta z = 0$). $M_{in} = 0.65$; 3D rig configuration with side-walls (RANS with $k\omega - SST$ turbulence model)

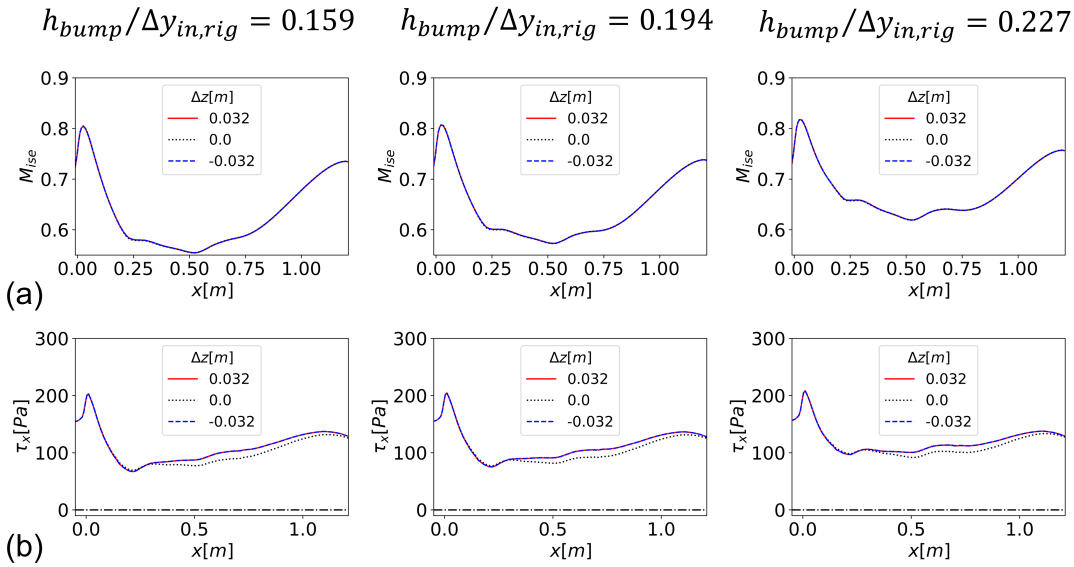


Fig. 15 Effect of a change in bump geometry on (a) isentropic Mach number and (b) axial wall shear stress distributions on the lower wall at different spanwise positions relative to mid-span ($\Delta z = 0$). $M_{in} = 0.65$; 3D rig configuration with side-walls (RANS with $k\omega - SST$ turbulence model)

The effect of the blockage due to the side-wall boundary layers and corner flows on the characteristics of the flow over the fan cowl was assessed through the comparison between the 2D-planar and 3D with side-walls analyses (Fig. 16). At mid span ($\Delta z = 0$), the pre-shock Mach number on the forebody of the fan cowl and the separation extent were only slightly affected. For example, for the configuration $h_{bump}/\Delta y_{in,rig} = 0.227$ the pre-shock Mach number for the 2D-planar case was 1.62 whereas it was about 1.6 for the 3D configuration with side-walls. The increase in spanwise extent of the corner flows at the side-walls produced further blockage on the afterbody that led to a slightly higher post-shock isentropic Mach number for the 3D configuration with side-walls compared to the 2D-planar model (Fig.

16). Overall, the presence of the side-walls did not significantly affect the characteristics of the flow at mid-span and the 2D-planar model was a useful design approach for the diversion configuration.

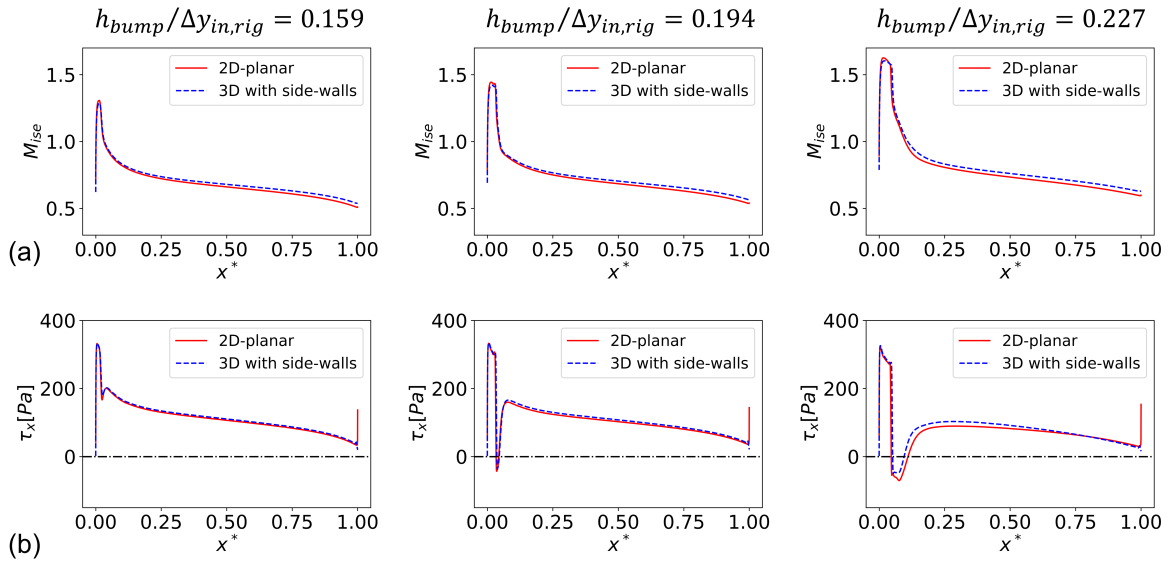


Fig. 16 Effect of blockage and secondary flows due to the side-walls of he rig on (a) isentropic Mach number and (b) axial wall shear stress distributions on the nacelle fan cowl. Profiles for the 3D with side-walls computations taken at mid-span ($\Delta z = 0$). $M_{in} = 0.65$; 2D-planar model and 3D with side-walls (RANS with $k\omega - SST$ turbulence model)

The achievable Reynolds number within the rig was about 3 times lower compared to the one representative of a full-size engine nacelle under windmilling diversion conditions. Thus, the boundary layer characteristics for the quasi-2D configuration were determined through 3D CFD studies with side-walls and the $\gamma - Re_\theta$ as the turbulence model. When the transitional characteristics of the boundary layer were taken into account, the boundary layer on the nacelle aeroline was separated for all the configurations with the different bump geometries (Fig. 17). For the lower bump height ($h_{bump}/\Delta y_{in,rig} = 0.159$), the pre-shock Mach number was 1.28 and there was a laminar separation that induced transition to a turbulent boundary layer which then reattached before the foot of the near-normal shock (Fig. 17). Similarly, for the configuration $h_{bump}/\Delta y_{in,rig} = 0.194$ there was laminar separation and reattachment of the boundary layer ahead of the shock. On the other hand, for the configuration $h_{bump}/\Delta y_{in,rig} = 0.227$ there was transition of the boundary layer ahead of the shock and a closed fully turbulent shock-induced separation (Fig. 17). Compared to to the 3D annular case, under the rig configuration the nacelle may exhibit slightly different characteristics of the boundary layer. Nevertheless, the limitations of correlation-based transitional turbulence model are well known and therefore the analysis highlighted the need for experimental data where the status of the boundary layer ahead of the shock can be monitored. In addition, the computations showed that it may be necessary to force the transition of the boundary layer to achieve attached conditions for the lower bump height ($h_{bump}/\Delta y_{in,rig} = 0.159$). This will be further investigated within the experiments by means of a nacelle aeroline with different roughness profiles.

2. Windmilling EoR

The development of the EoR configuration closely followed the philosophy of the diversion configuration. The topline ($\phi = 0^\circ$) of the nacelle cowl was used for the rig configuration as there was onset of boundary layer separation at $\phi = 0^\circ$ for the 3D-annular configuration under windmilling EoR conditions (Fig. 8). Several bump geometries were used to control the mass flow split within the rig, with an overall change in bump height relative to the nominal design condition of $0.07\Delta y_{in,rig}$ (Fig. 18). Around the separation point, the bump height was increased by approximately $0.004\Delta y_{in,rig}$ to capture the onset of separation (Fig. 19). When the boundary layer on the nacelle aeroline separates, the increased area blockage due to the separation on the lower channel redistributes the mass flow through the upper channel and the mass flow ratio between lower and upper channel ($\dot{m}_{lc}/\dot{m}_{uc}$) decreases (Fig. 19).

For the lower bump height ($h_{bump}/\Delta y_{in,rig} = 0.286$), the boundary layer was attached and the peak isentropic Mach

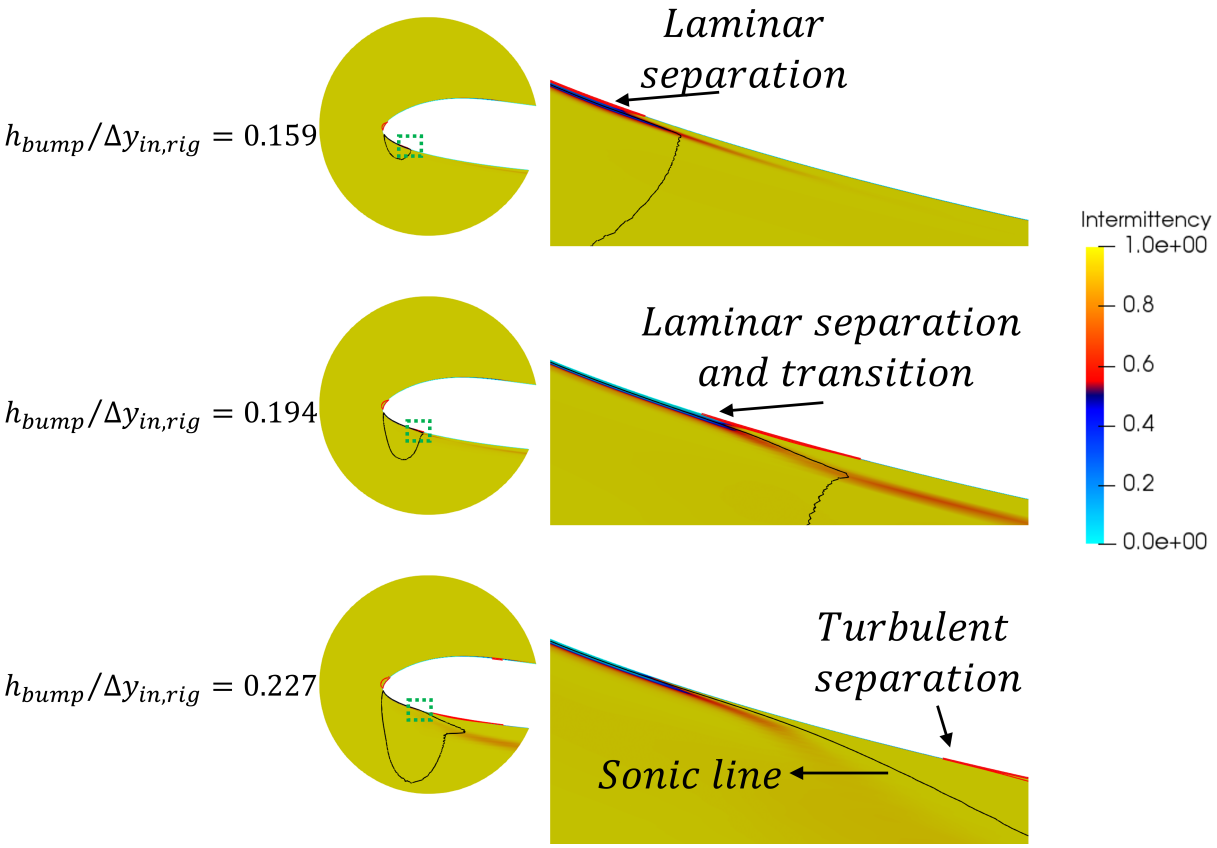


Fig. 17 Effect of change in bump geometry on the characteristics of the separation on the nacelle fan cowl. Intermittency distribution at mid-span ($\Delta z = 0$). $M_{in} = 0.65$; 3D with side-walls model (RANS with $\gamma - Re_\theta$ turbulence model)

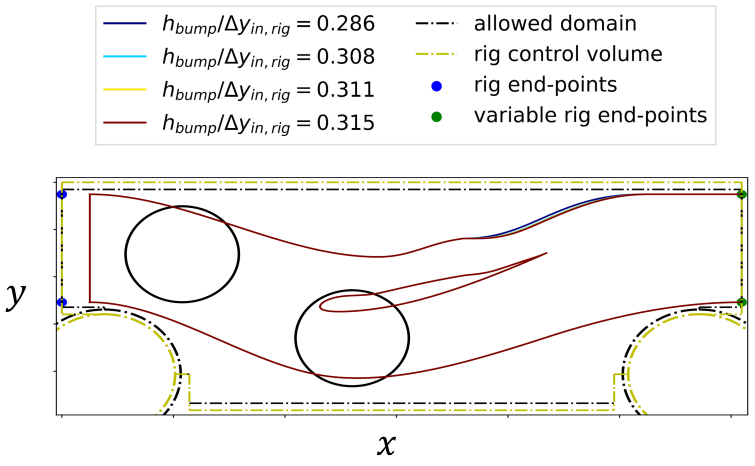


Fig. 18 Schematic of the rig configuration for the EoR condition and bump geometries used to control the mass flow split

number at mid-span was $M_{ise,max} \approx 0.85$ (Fig. 20a,b). The peak isentropic Mach number increased to $M_{ise,max} \approx 0.9$ for $h_{bump}/\Delta y_{in,rig} = 0.311$ and the boundary layer on the nacelle aerolne was still attached (Fig. 20a,b). A further

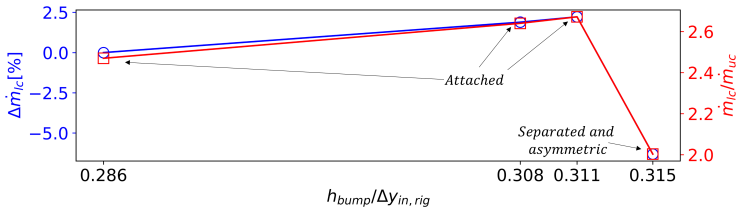


Fig. 19 Effect of a change in bump height on non-dimensional massflow split within the channel (red) and mass flow through the lower channel (blue). $M_{in} = 0.25$; 3D with side-walls model (RANS with $\gamma - Re_\theta$ turbulence model)

increase in bump height ($h_{bump}/\Delta y_{in,rig} = 0.315$) separated the boundary layer and the peak isentropic Mach number reduced to approximately 0.64 (Fig. 20a,b). Compared to the 3D-annular case (Fig. 9c)), the axial distribution of the Stratford coefficient on the nacelle aeroline (Fig. 20c) for the attached case was similar on the nacelle forebody, but it was significantly different on the nacelle afterbody. In particular, F_s was greater under the rig configuration, which indicates a greater diffusion level. Despite the attempt to modify the lower wall of the rig to reduce the adverse pressure gradient on the nacelle afterbody, it was not possible to replicate the 3D-annular configuration. Although the amplitude of the pressure gradient on the nacelle afterbody affected the separation onset of the boundary layer, the characteristics and mechanisms were similar to the 3D-annular configuration. Thus, the rig configuration was considered to be sufficiently representative of the 3D-annular one.

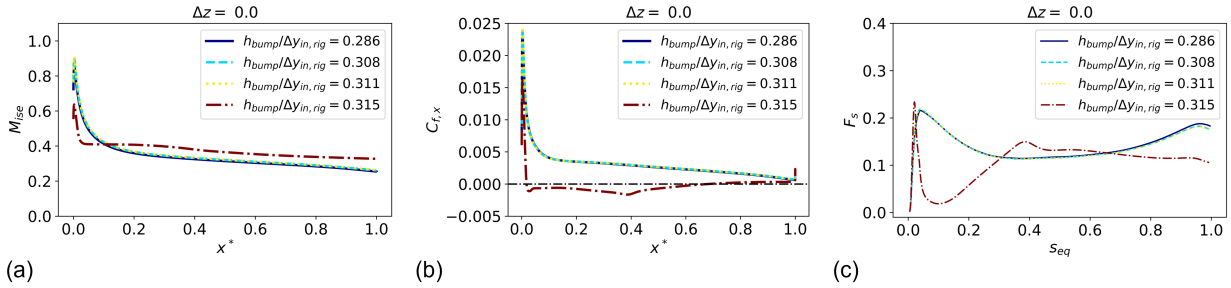


Fig. 20 Effect of a change in bump height on (a) isentropic Mach number, (b) wall axial skin friction coefficient and (c) Stratford coefficient axial distributions on the fan cowl at mid-span ($\Delta z = 0$). 3D with side-walls model (RANS with $k\omega - SST$ turbulence model)

Due to the convoluted shapes of the liners of the wind tunnel configuration, the three-dimensionality of the flow was significant. Towards the exit of the working section there were two counter-rotating vortices on the upper wall (Fig. 21) that were initiated by the notable changes in streamwise curvature on the duct. Thus, the effect of the secondary flows on the separation onset and characteristics of the boundary layer on the nacelle cowl was investigated. Computations with inviscid wall boundary conditions on the wind tunnel walls were used. The separation onset was not influenced by the boundary layer developments on the wind tunnel wall (Fig. 22) and the separation was still driven by a diffusion mechanism.

For the final rig configuration, the effect of the aerodynamic incidence angle (α) of the nacelle aeroline on the characteristics of the boundary layer was investigated. The reference aerodynamic incidence angle (α_{ref}) corresponded to the geometrical incidence angle (α_g). The centre of rotation for the aerodynamic incidence angle was approximately located at the position of the notional fan face (Fig. 23). As anticipated in section III.A.2, a change in α within the rig is accompanied by a change in the mass flow split between the upper and lower channel as the rig walls are kept the same (Fig. 24). Relative to the reference design point (α_{ref}) and for the lower bump height ($h_{bump}/\Delta y_{in,rig} = 0.286$), α was decreased and increased by 1° and 2°, respectively. For the final configuration, it was possible to vary α by approximately 2° and achieve attached and separated conditions (Fig. 24). Thus, the range of α may be sufficiently large to cover the range of interest within a 3D-annular configuration (Fig. 10).

Compared to the diversion configuration, for the EoR one the boundary layer on the nacelle aeroline was significantly

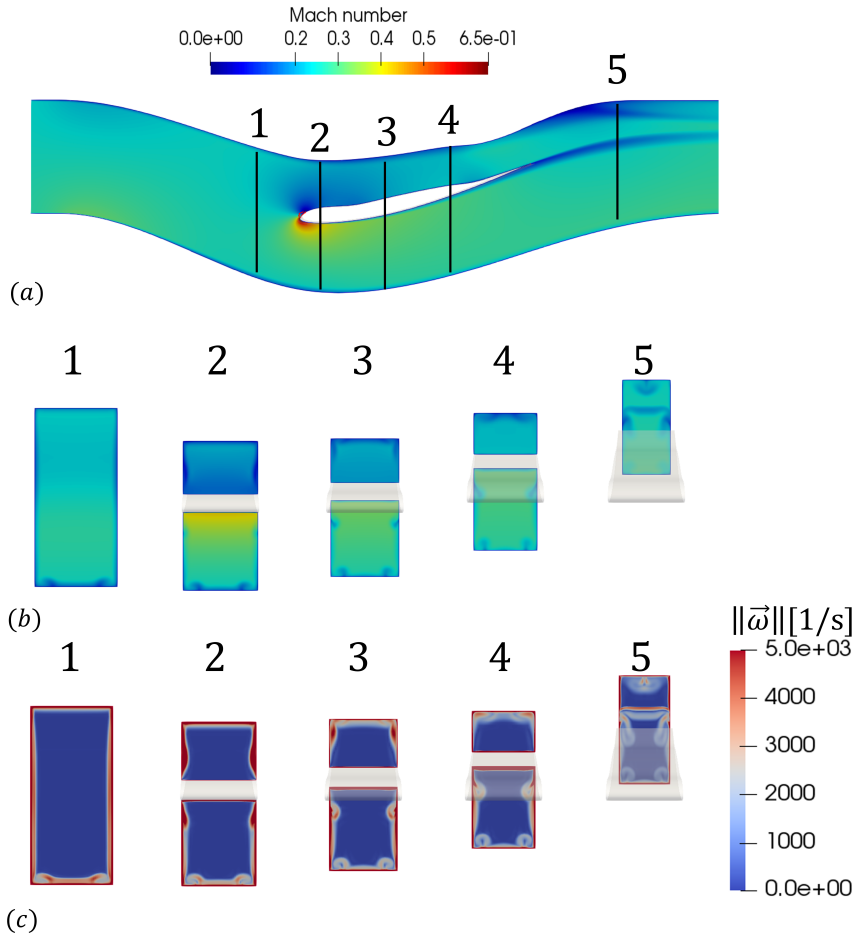


Fig. 21 (a) Mach number distribution on a meridional plane at mid-span ($\Delta z = 0$); (b) Mach number and (c) vorticity magnitude distributions on cross-sectional views at axial positions marked in (a). $h_{bump}/\Delta y_{in,rig} = 0.286$, $M_{in} = 0.25$; 3D with side-walls model (RANS with $k\omega - SST$ turbulence model)

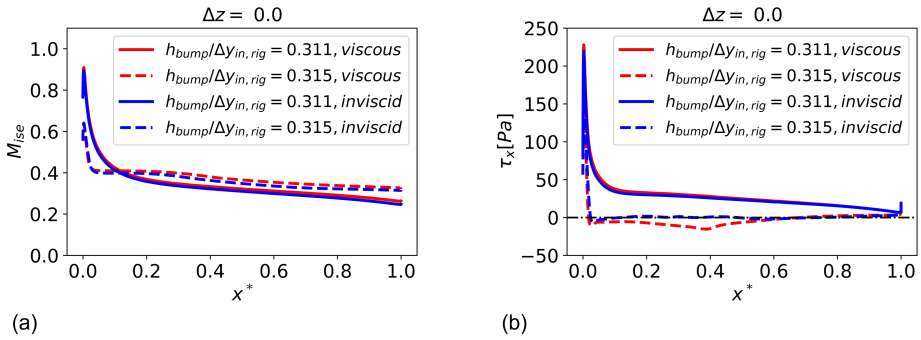


Fig. 22 Effect of boundary layer on the wind tunnel walls on (a) isentropic Mach number and (b) axial wall-shear stress distributions on the fan cowl at mid-span ($\Delta z = 0$). $M_{in} = 0.25$; 3D with side-walls model (RANS with $k\omega - SST$ turbulence model)

more sensitive to changes in bump height. A small increase in bump height ($0.07\Delta y_{in,rig}$) was sufficient to move from an attached condition to a greatly separated one where the flow within the rig was not symmetric relative to mid-span (Fig. 25). The latter may be related to the onset of flow unsteadiness that cannot be captured through a

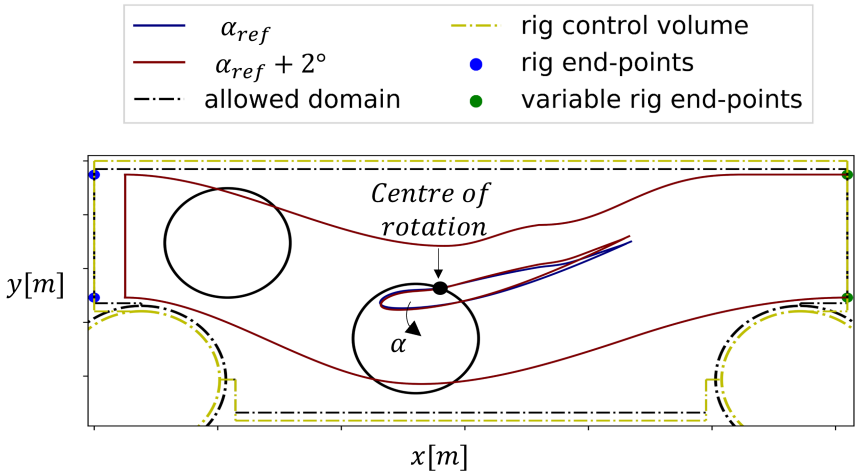


Fig. 23 Schematic of the effect of a change of the aerodynamic incidence angle on the rig configuration

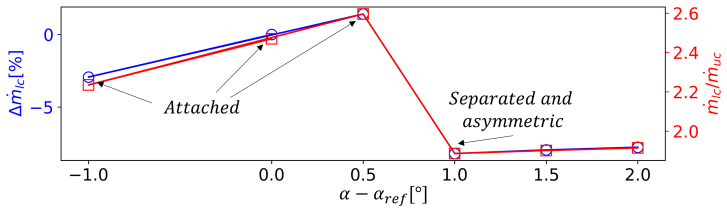


Fig. 24 Effect of a change in aerodynamic incidence angle of the nacelle aeroline on non-dimensional massflow split within the channel (red) and mass flow through the lower channel (blue). $h_{bump}/\Delta y_{in,rig} = 0.286$**,** $M_{in} = 0.25$**; 3D with side-walls model (RANS with** $k\omega - SST$ **turbulence model)**

steady RANS methods. Thus, the rig configuration may not be able to capture the separation mechanism as the change in bump geometry cannot be done in a 'continuous' manner, but it would conversely requires separate wind tunnel runs. Thus, a change in inlet Mach number was investigated as an alternative way to separate the boundary layer and capture the transition from one state to the other. For a non-dimensional bump height $h_{bump}/\Delta y_{in,rig} = 0.340$, M_{in} was progressively increased from $M_{in} = 0.2$ to 0.3 and the boundary layer transitioned from attached to separated (Fig. 26). For $M_{in} = 0.275$ the peak isentropic Mach number was supersonic ($M_{ise,max} \approx 1.21$) and significantly greater compared to the 3D-annular case. Nevertheless, it is believed that the separation of the boundary layer ($M_{in} = 0.3$) was still driven by a diffusion mechanism as the separation characteristics were similar (Fig. 27) to what previously observed for a $M_{in} = 0.25$ (Fig. 25). Thus, a change in inlet Mach number may be used within the experiments to capture the separation mechanism representative of a nacelle under windmilling EoR conditions.

IV. Conclusion

Overall, two canonical rig configurations were developed to assess the detailed characteristics of the nacelle boundary layer at diversion and end of runway windmilling conditions. The two configurations met the key design requirements. For the diversion configuration, the flow at mid-span was sufficiently 2D dimensional and therefore a 2D-planar design process was appropriate. Conversely, for the EoR configuration, a 3D design approach was required. However, the influence of the boundary layer development on the wind tunnel side-walls did not fundamentally changed the separation characteristics of the boundary layer on the nacelle aeroline. It is believed that the experimental data that will be obtained through the two rig configurations will enable the validation of CFD methods and mitigate the technical risks associated with the development of compact aero-engine nacelles for future ultra-high bypass ratio turbofan engines.

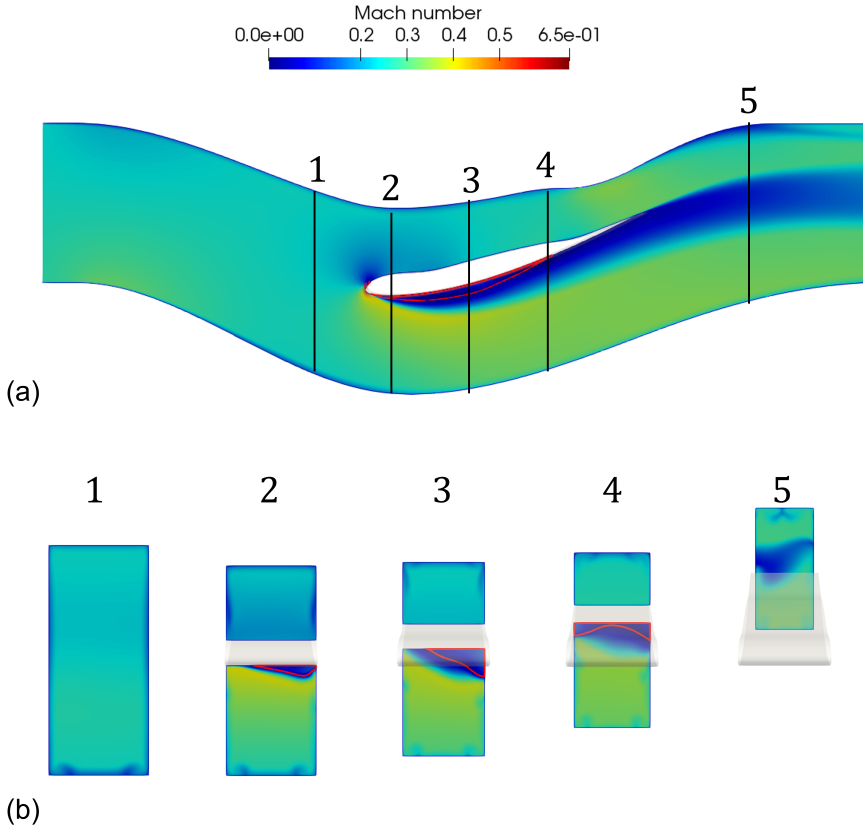


Fig. 25 (a) Mach number distribution on a meridional plane at mid-span ($\Delta z = 0$); (b) Mach number distribution on cross-sectional views at axial positions marked in (a). $h_{bump}/\Delta y_{in,rig} = 0.315$, $M_{in} = 0.25$; 3D with side-walls model (RANS with $k\omega - SST$ turbulence model)

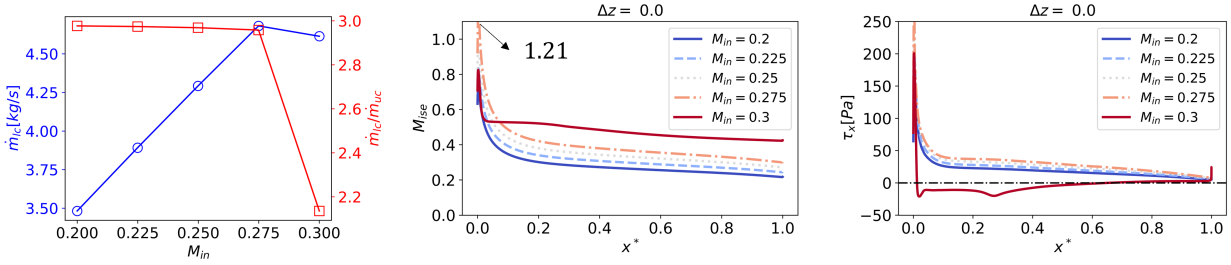


Fig. 26 (Effect of inlet Mach number on (a) mass flow split and lower channel mass flow, axial distributions of (b) isentropic Mach number and (c) axial wall-shear stress on the nacelle aeroline at mid-span ($\Delta z = 0$). $h_{bump}/\Delta y_{in,rig} = 0.340$; 3D with side-walls model (RANS with $k\omega - SST$ turbulence model)

Acknowledgments

This project has received funding from the Clean Sky 2 Joint Undertaking (JU) under grant agreement number 101007598. The JU receives support from the European Union's Horizon 2020 research and innovation programme and the Clean Sky 2 JU members other than the Union.

Data availability statement

Due to commercial confidentiality agreements the supporting data are not available.

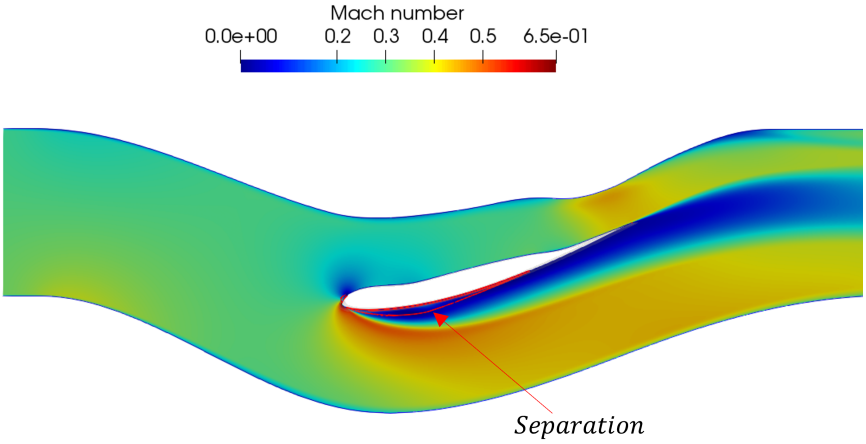


Fig. 27 Mach number distribution on a meridional plane at mid-span ($\Delta z = 0$). Red solid line: $V_x = 0$. $h_{bump}/\Delta y_{in,rig} = 0.340$, $M_{in} = 0.3$; 3D with side-walls model (RANS with $k\omega - SST$ turbulence model)

References

[1] Hughes, C. E., "Aircraft engine technology for green aviation to reduce fuel burn," *3rd AIAA Atmospheric Space Environments Conference*, , No. June 2011, 2011, pp. 1–18. https://doi.org/10.2514/6.2011-3531.

[2] Tejero, F., Robinson, M., MacManus, D. G., and Sheaf, C., "Multi-objective optimisation of short nacelles for high bypass ratio engines," *Aerospace Science and Technology*, Vol. 91, 2019, pp. 410–421. https://doi.org/10.1016/j.ast.2019.02.014.

[3] Tejero, F., Christie, R., MacManus, D., and Sheaf, C., "Non-axisymmetric aero-engine nacelle design by surrogate-based methods," *Aerospace Science and Technology*, Vol. 117, 2021, p. 106890. https://doi.org/10.1016/j.ast.2021.106890, URL https://doi.org/10.1016/j.ast.2021.106890.

[4] Robinson, M., MacManus, D. G., Christie, R., Sheaf, C., and Grech, N., "Nacelle design for ultra-high bypass ratio engines with CFD based optimisation," *Aerospace Science and Technology*, Vol. 113, 2021, p. 106191. https://doi.org/10.1016/j.ast.2020.106191, URL https://doi.org/10.1016/j.ast.2020.106191.

[5] Deneys Schreiner, B. J., Tejero, F., MacManus, D. G., and Sheaf, C., "Robust aerodynamic design of nacelles for future civil aero-engines," *Proceedings of the ASME Turbo Expo*, Vol. 1, No. M, 2020, pp. 1–11. https://doi.org/10.1115/GT2020-14470.

[6] Swarthout, A., MacManus, D., Tejero, F., Matesanz-García, J., Boscagli, L., and Sheaf, C., "A comparative assessment of multi-objective optimisation methodologies for aero-engine nacelles," ICAS, 2022.

[7] Sánchez Moreno, F., MacManus, D., Hueso Rebassa, J., Tejero, F., and Sheaf, C., "Optimization of installed compact and robust nacelles using surrogate models," ICAS, 2022.

[8] Chiles, P., "ETOPS redefined," *AeroSafety World*, Vol. 2, No. 3, 2007, pp. 88–92.

[9] Makuni, T. E., Babinsky, H., Slaby, M., and Sheaf, C., "Experimental investigations of shock-wave/boundary-layer interactions in transonic aircraft engine intakes at high incidence," *53rd AIAA Aerospace Sciences Meeting*, , No. January, 2015. https://doi.org/10.2514/6.2015-0067.

[10] Coschignano, A., and Babinsky, H., "Boundary-Layer Development Downstream of Normal Shock in Transonic Intakes at Incidence," *AIAA Journal*, Vol. 57, No. 12, 2019, pp. 5241–5251. https://doi.org/10.2514/1.j058508.

[11] O'Pray, C. E., Babinsky, H., and Sheaf, C., "The Influence of Surface Geometry on the Fan-Plane Boundary-Layer in Transonic Intakes at High-Incidence," *AIAA SCITECH 2022 Forum*, 2022, p. 1806. https://doi.org/https://doi.org/10.2514/6.2022-1806.

[12] Coschignano, A., Atkins, N., Babinsky, H., and Serna, J., "Effect of Reynolds number on a normal shock wave-transitional boundary-layer interaction over a curved surface," *Experiments in Fluids*, Vol. 60, No. 12, 2019, pp. 1–12. https://doi.org/10.1007/s00348-019-2824-0, URL https://doi.org/10.1007/s00348-019-2824-0.

[13] Coles, C., Babinsky, H., and Sheaf, C., "The impact of roughness size on the shock wave-boundary-layer interaction on aero-engine intakes at incidence," *AIAA Scitech 2019 Forum*, 2019, pp. 1–13. https://doi.org/10.2514/6.2019-0296.

[14] Hoelmer, W., Younghans, J. L., and Raynal, J. C., "Effect of Reynolds number on upper cowl flow separation," *Journal of Aircraft*, Vol. 24, No. 3, 1987, pp. 161–169. https://doi.org/10.2514/3.45411.

[15] Younghans., Hoelmer, W., and Stockman, N., "Low speed effects of Reynolds number and lip geometry on high bypassratio inlet performance," 1982. https://doi.org/10.2514/6.1982-59.

[16] ANSYS Inc, "ANSYS FLUENT User's Guide," Tech. rep., Canonsburg, PA 15317, 2019.

[17] Menter, F. R., Kuntz, M., and Langtry, R., "Ten years of industrial experience with the SST turbulence model," *Turbulence, heat and mass transfer*, Vol. 4, No. 1, 2003, pp. 625–632.

[18] Christie, R., Heidebrecht, A., and MacManus, D., "An automated approach to nacelle parameterization using intuitive class shape transformation curves," *Journal of Engineering for Gas Turbines and Power*, Vol. 139, No. 6, 2017, pp. 1–9. https://doi.org/10.1115/1.4035283.

[19] Celik, I. B., Ghia, U., Roache, P. J., Freitas, C. J., Coleman, H., and Raad, P. E., "Procedure for estimation and reporting of uncertainty due to discretization in CFD applications," *Journal of Fluids Engineering, Transactions of the ASME*, Vol. 130, No. 7, 2008, pp. 0780011–0780014. https://doi.org/10.1115/1.2960953.

[20] Jiménez, J., "Intermittency in Turbulence," *Encyclopedia of Mathematical Physics*, edited by J.-P. Françoise, G. L. Naber, and T. S. Tsun, Academic Press, Oxford, 2006, pp. 144–151. https://doi.org/https://doi.org/10.1016/B0-12-512666-2/00368-0, URL https://www.sciencedirect.com/science/article/pii/B0125126662003680.

[21] Stratford, B., "The prediction of separation of the turbulent boundary layer," *Journal of fluid mechanics*, Vol. 5, No. 1, 1959, pp. 1–16.

[22] Gerhart, P. M., and Bober, L. J., "Comparison of several methods for predicting separation in a compressible turbulent boundary layer," Tech. Rep. TM X-3102, NASA, 1974.

[23] Cebeci, T., Mosinskis, G., and Smith, A., "Calculation of separation points in incompressible turbulent flows," *Journal of Aircraft*, Vol. 9, No. 9, 1972, pp. 618–624.

[24] Goulos, I., MacManus, D., Hueso Rebassa, J., Tejero, F., Au, A., and Sheaf, C., "Impact of Installation on the Performance of an Aero-Engine Exhaust at Wind-Milling Flow Conditions," *Proceedings of the ASME Turbo Expo*, 2023.



https://dspace.org/

Design of a quasi-2D rig configuration to assess nacelle aerodynamics under windmilling conditions

Boscagli, Luca; Tejero, Fernando; Swarthout, Avery E.; MacManus, David G.; Sabnis, Kshitij ...

2023-06-08
American Institute of Aeronautics and Astronautics (AIAA)
https://doi.org/10.2514/6.2023-3392
Boscagli L, Tejero F, Swarthout AE, et al., (2023) Design of a quasi-2D rig configuration to assess nacelle aerodynamics under windmilling conditions. In: 2023 AIAA Aviation and Aeronautics Forum and Exposition (AIAA AVIATION Forum), 12-16 June 2023, San Diego, USA. Paper number AIAA 2023-3392

Downloaded from a DSpace repository. https://dspace.org/